

High Dynamic Range Probing of Single-Molecule Mechanical Force Transitions at Cell–Matrix Adhesion Bonds by a Plasmonic Tension Nanosensor

Shaojun Wu,[†] Wenjing Tang,[†] Ziyi Wang, Zhuodong Tang, Peng Zheng,* Zixuan Chen,* and Jun-Jie Zhu*



Cite This: *JACS Au* 2024, 4, 1155–1165



Read Online

ACCESS |

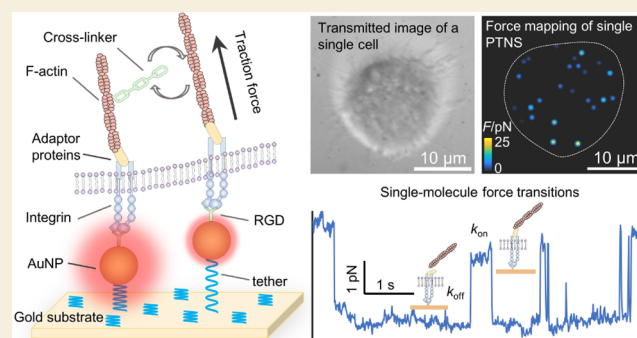
Metrics & More

Article Recommendations

Supporting Information

ABSTRACT: Mechanical signals in animal tissues are complex and rapidly changed, and how the force transduction emerges from the single-cell adhesion bonds remains unclear. DNA-based molecular tension sensors (MTS), albeit successful in cellular force probing, were restricted by their detection range and temporal resolution. Here, we introduced a plasmonic tension nanosensor (PTNS) to make straight progress toward these shortcomings. Contrary to the fluorescence-based MTS that only has specific force response thresholds, PTNS enabled the continuous and reversible force measurement from 1.1 to 48 pN with millisecond temporal resolution. We used the PTNS to visualize the high dynamic range single-molecule force transitions at cell–matrix adhesions during adhesion formation and migration. Time-resolved force traces revealed that the lifetime and duration of stepwise force transitions of molecular clutches are strongly modulated by the traction force through filamentous actin. The force probing technique is sensitive, fast, and robust and constitutes a potential tool for single-molecule and single-cell biophysics.

KEYWORDS: *mechanic force nanosensors, single-cell analysis, single-molecule detection, cell adhesions, microscopy*



INTRODUCTION

Force transmission at the interface between cells and the extracellular matrix (ECM) plays a crucial role in regulating physiological processes and cellular functions.^{1–3} Focal adhesions (FAs) are multimolecular complexes that link filamentous (F) actin to the extracellular matrix and transmit a mechanical force. Measuring the mechanical forces of whole cells is insufficient to fully understand how FA-mediated force transmission occurs and to study the underlying mechanical mechanisms.^{4–9} To address this challenge, molecular tension sensors (MTS) based on fluorescence resonance energy transfer (FRET) have been developed to enable single-molecule force measurement during adhesion formation.^{2,10–12} The high sensitivity of these sensors relies on narrow-gap-dependent FRET efficiency, which, unfortunately, limits the detection range. Efforts have been made in recent years to develop an advanced MTS to overcome this limitation. For example, a series of FRET-based MTSs were synthesized to expand the detection range together.^{13–15} Although effective, these multiprobe strategies are unable to measure continuous force evolution. To date, a method permitting high dynamic range force measurement is still lacking. Additionally, fluorescence-based MTS cannot balance long-term detection

of force changes with high temporal resolution due to phototoxicity and photobleaching limitations.¹² For instance, the binding and detachment processes between cells and substrates that cause tension changes usually occur within a time frame of 100 ms.¹⁶ However, single-molecule FRET-based probes typically cannot achieve the necessary temporal resolution for extended periods.¹⁷

To solve the above challenges, finding a novel distance response solution as an alternative to fluorescent labeling would be a feasible approach. Recently, plasmonic resonance scattering of noble metal nanomaterials has attracted significant attention in the detection of chemical and biological systems because of their stable and sensitive scattering.^{18–21} Plasmonic nanoprobe, known for their continuous high sensitivity to the distance from substrates, have also been employed in single-molecule detection.^{22–24} For example,

Received: January 2, 2024
Revised: January 30, 2024
Accepted: February 1, 2024
Published: February 19, 2024



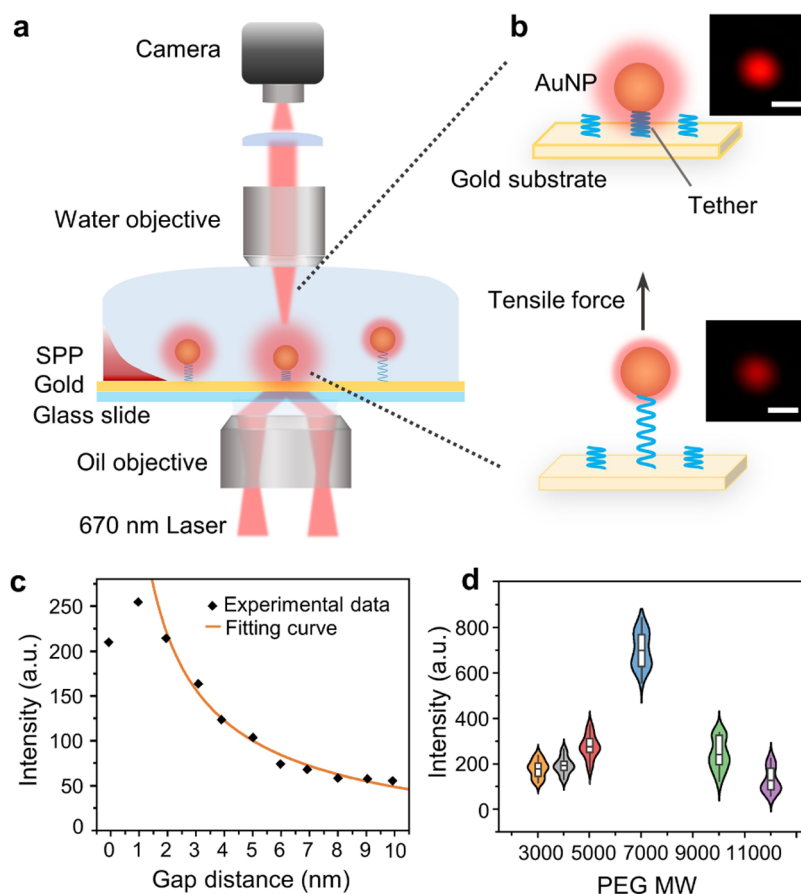


Figure 1. Principle of plasmonic molecular tension nanosensors. (a) Schematic illustration of the optical setup of the plasmonic scattering microscope. (b) Schematic illustration of the force detection using scattering intensity changes of the PTNS. Insets: scattering images of a single PTNS before and after the application of force, respectively. The scale bar is 500 nm. (c) Gap distance dependence of the scattering intensity (diamonds) of a single PTNS and the power-law fitting curve (yellow curve). (d) Molecular weight dependence of the scattering intensity of the PTNS ($n = 30$).

plasmonic scattering microscopy was used to measure subnanometer-scale gap distance variation between a single gold nanoparticle (AuNP) and a gold surface.²⁵ The combination of MTS with distance-sensitive plasmonic nanoprobe presents a potential solution for the rapid, sensitive, and durable assessment of mechanical forces in cells.

In this work, we sought to develop a plasmonic tension nanosensor (PTNS) for dynamically probing single-molecule mechanical forces in living cells. We reported a correlation between the plasmonic-coupled scattering intensity of a poly(ethylene glycol) (PEG)-tethered AuNP and the applied tensile force, which followed the worm-like chain (WLC) model. Calibration experiments using an atomic force microscope (AFM) confirmed that PTNS has a wide detection range from 1.1 to 48 pN, making it an effective tool for studying integrin-ligand force dynamics ranging from 1 to 50 pN.^{12,26–28} Due to its robust plasmonic scattering, PTNS significantly advances temporal resolution by enabling measurement of force transitions at the millisecond level throughout the entire cell adhesion process. These single-molecule force transitions are consistent with the predicted modified molecular clutch model¹² and reveal that the traction force along the F-actin regulates the lifetime and transition time of force transitions in molecular clutches within living cells. Furthermore, the study combines traction force distribution and cell boundary expansion to unveil the

correlation between cell movement direction and local mechanical force in NIH-3T3 cells, although this correlation is still under dispute in other cell lines.²⁹

METHODS

A detailed description of the experimental procedures is documented in the [Supporting Information](#). Briefly, gold nanoparticles with a size of 70 nm were synthesized and attached to the Au film by PEG elasticity molecules. Transmission electron microscopy (TEM) was used to observe the size and shape of the gold nanoparticles. Scanning electron microscopy (SEM) was used to characterize the assembly of PTNS to confirm that the gold nanoparticles were uniformly and monodispersely distributed on the surface of the Au film. The change of scattering intensity when the gap distance between the gold nanoparticle and the Au film was determined by experiment and finite-difference time-domain (FDTD) simulations. Force–extension curves of the probe were obtained using an atomic force microscope (AFM).

RESULTS AND DISCUSSION

Configuration and Work Principle of Plasmonic Tension Nanosensors

The construction of the PTNS is illustrated in [Figure 1a](#). A 47 nm thick Au film was coated on a cover slide (see the [Methods](#) section). Individual gold nanoparticles (AuNPs) with a diameter of 70 nm ([Figure S1](#)) were uniformly modified on the Au film, tethered by elastic poly(ethylene glycol) (PEG)

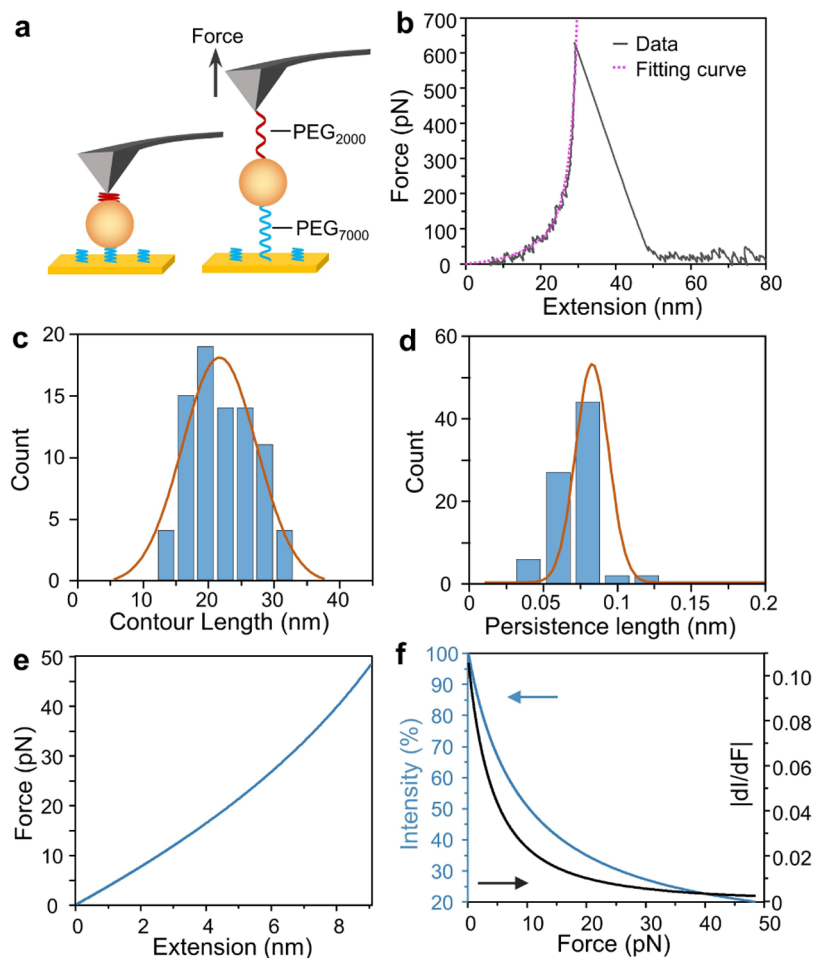


Figure 2. Calibration and performance characterization. (a) Schematic illustration of the setup for the force–extension curve measurement. (b) Force–extension curve of the whole force system (solid curve) and fitting curve (dashed curve) using the series worm-like chain (WLC) model. (c, d) Histograms illustrating the distribution of contour length and persistence length calculated from the force–extension curves ($n = 81$). (e) Calculated force–extension curve of bottom PEG₇₀₀₀. (f) Plots of the relative scattering intensity (blue curve) and the sensitivity (dark curve) as a function of the tensile force loads on the PTNS.

molecules (Figure S2). The PEG molecules served as flexible linkers, which were folded in a relaxed conformation without force, bringing the AuNPs close to the gold surface. Upon the application of a tensile force, the linkers extended, separating the AuNPs from the Au film. A homemade plasmonic scattering microscopy was used to measure the extension of single PTNS and probe the tensile force.^{25,30,31} This microscopy consisted of a coaxial dual-objective setup with an inverted high numerical aperture oil immersion objective below and an upright water immersion objective above. The PTNS was placed between these objectives. A p-polarized 670 nm light was incident onto the Au film at a critical angle, generating a surface plasmon polariton (SPP) wave near the gold surface. Single PTNS scattered the SPP wave, and the scattering light was captured by an upright objective to form scattering images. The scattering intensity of a PTNS is determined by the SPP wave and the scattering cross section of the AuNP, both of which depend on the gap distance z .²⁵ The scattering intensity decreases rapidly when a tensile force is applied, and the AuNP is pulled away from the gold surface (Figure 1b). The relative scattering intensity (I) can be expressed as

$$I \sim |E_p(z)|^2 C_{sca}(z) \quad (1)$$

where $E_p(z)$ and $C_{sca}(z)$ are the excited SPP wave and the scattering cross section of an AuNP at a gap distance z from the gold surface, respectively. When z is between 0 and 10 nm, the change in $E_p(z)$ is much smaller than in $C_{sca}(z)$, so the change in scattering intensity is primarily determined by $C_{sca}(z)$.²⁵

To calibrate the z -dependent scattering intensity of a PTNS, a single AuNP was moved in the z -direction from 0 to 10 nm with a step size of 1 nm (Figure S3). Figure 1c shows that the scattering intensity exhibited two distinct trends before and after 1 nm. The scattering intensity increased when the gap distance increased from 0 to 1 nm, and then rapidly decreased. The fitting curve in the range from 2 to 10 nm indicated a power-law relationship between the scattering intensity and the gap distance. This can be attributed to the coupling effect between the gold surface and AuNPs.³² As an AuNP approached the gold surface, its scattering spectrum became red-shifted, which followed a power-law relationship (Figure S4). Therefore, the maximum scattering intensity occurred at 1 nm, with the peak wavelength fitting the incident light (~ 670 nm). To prevent the abnormal trend from influencing the power-law relationship between the scattering intensity and the gap distance, the length of the PEG elastic molecules was optimized. Figure 1d shows the scattering intensity distribu-

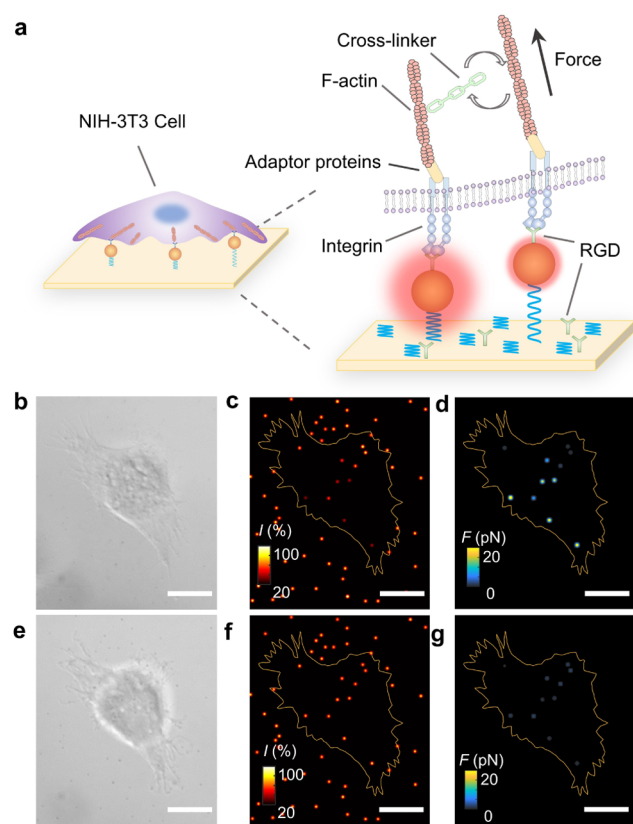


Figure 3. Measurement of local traction force in individual living cells. (a) Schematic illustration of the formation of cell tension. (b–d) Transmitted (b), scattering (c), and force images (d) of a single NIH-3T3 cell incubated with PTNS. The scale bar is 10 μm. (e–g) Transmitted (e), scattering (f), and force images (g) of the cell in (b–d) after treated by cytochalasin D for 5 min. The scale bar is 10 μm.

tions of at least 30 PTNS tethered by PEG with different molecular weights. The 7000 Da molecular weight was selected because the scattering intensity exhibited inverse trends before and after it. This implied that among these molecular weights, the scattering intensity of PTNS-modified PEG with 7000 Da molecular weight was closest to the peak intensity. The scattering spectra of these PTNS showed a concentrated distribution at around 630 nm (Figure S5), suggesting that further extension would result in power-law decay in the scattering intensity.

To determine the tensile force, atomic force microscopy (AFM) was used to correlate the force and extension of PEG.³³ In the experiments, an azide-modified AFM cantilever initially approached the alkyne-PEG₂₀₀₀-modified AuNP and maintained a set point of ~300 pN for 5 s. The experiment was conducted in a 50% (v/v) *t*-BuOH/H₂O solution containing 100 μM CuSO₄ and 1 mM sodium ascorbate to catalyze the click reaction between the azide and alkyne groups. In the presence of Cu(I), the cantilever captured the alkyne-PEG₂₀₀₀ on top of the AuNP via the copper-catalyzed azide–alkyne cycloaddition (CuAAC) click reaction and retracted under a constant velocity, causing the movement of the AuNP (Figure 2a). After retraction, the force–extension curve of the force system was obtained (Figure 2b). These force–extension curves exhibited only one rupture peak, which represented the desorption of the probe from the AuNP. Rupture events below 1 nN may not be induced by the reverse reaction of the CuAAC click reaction.³⁴ Regardless of the rupture site, the

PEG was mechanically stretched, triggering a movement of the AuNP. The force system consisted of PEG₂₀₀₀ on top and PEG₇₀₀₀ underneath the AuNP.^{35,36} The force–extension curve of the force system was fitted by the worm-like chain (WLC) model (Figure 2b, purple curve).^{37–39} More details of the fitting curve are shown in the Supporting Information. The range below 100 pN was preferred for fitting because bond angle deformations dictated the profile and the model was no longer valid above 100 pN.³⁹ Considering the working principle of the PTNS, the force–extension curve of the bottom PEG₇₀₀₀ was directly related to the gap distance *z* and was obtained by subtracting the extension of the top PEG₂₀₀₀ from the entire force system. A total of 81 force–extension curves of a single PTNS were collected to calculate the force–extension curve of the bottom PEG₇₀₀₀. The mean contour length was fitted to be 21.2 ± 8.1 nm (Figure 2c), and the persistence length was 0.083 ± 0.016 nm (Figure 2d). Deviations primarily arise from the variation in the chain number of PEG₇₀₀₀. These mean values provided a representative force–extension curve of bottom PEG₇₀₀₀ (Figure 2e). Based on the correlation of scattering and gap distance, the force load on a single PTNS can be expressed as (see the Methods section)

$$F(I) = \frac{k_B T}{L_p} \left[\frac{1}{4} \left(1 - \frac{k(I-a)^m - 2}{L_c} \right)^{-2} - \frac{1}{4} + \frac{k(I-a)^m - 2}{L_c} \right] \quad (2)$$

where k_B is the Boltzmann constant, T is the temperature in kelvin, L_p is 0.083 nm, L_c is 21.2 nm, and $k(I-a)^m - 2$ measures the extension with I , where k is 2.616 nm and m is −1.497.

Equation 2 describes the relationship between the tensile force and the relative scattering intensity (Figure 2f, blue curve). The range of relative scattering intensity was set from 100 to 20% because it exhibited an effective response to the gap distance in this range (Figure 1c). The sensitivity of the PTNS was determined by calculating the scattering intensity-dependent dI/dF . As shown in Figure 2f (dark curve), dI/dF varied from 0.106 to 0.003 pN^{−1}, as the tensile force increased from 0 to 48 pN. PTNS provided a high dynamic range for continuous force measurement, unlike the narrow detection range (several piconewtons) of fluorescently based single-molecule tension sensors (MTS). The detection limit of PTNS can be evaluated based on its highest sensitivity at the maximum scattering intensity for very small forces. The primary errors in force measurement came from either the persistence length or the scattering intensity. The broad distribution of the persistence length (0.083 ± 0.016 nm) indicated a ±19% relative standard deviation in force measurement. Accounting for the noise level of approximately 3.8% near the maximum scattering intensity (Figure S6), the detection limit of a PTNS was calculated to be 1.1 ± 0.21 pN (S/N = 3). This detection limit was one order smaller than the reported detection limit of AFM force spectroscopy (~10 pN)⁸ and similar to that of single-molecule FRET-based MTS (~2 pN).¹² Although still relatively coarse, it is suitable for measuring single-molecule tensile force at the pN level.

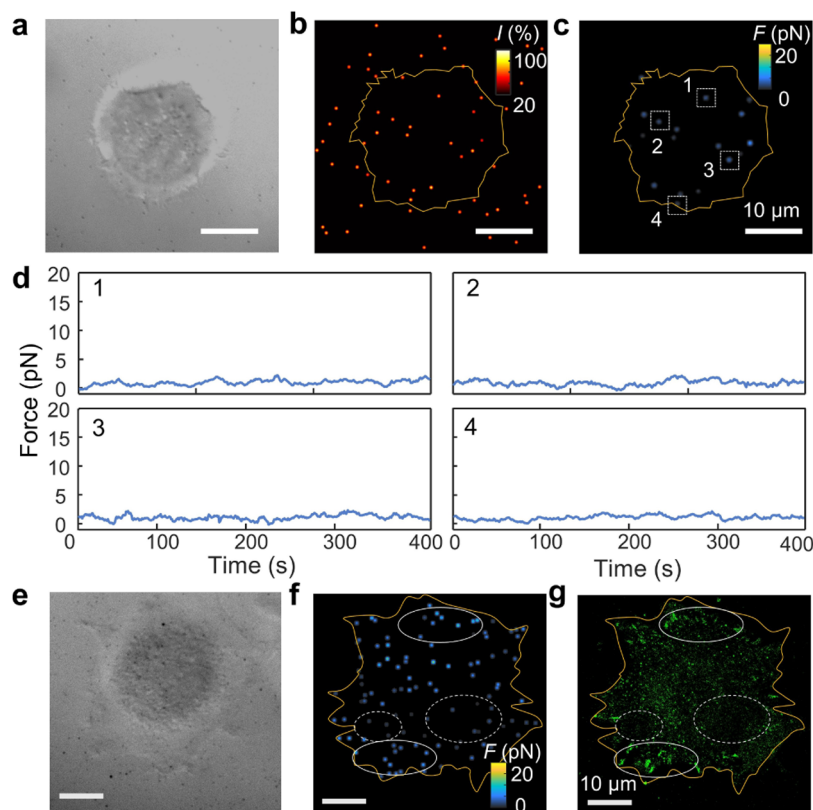


Figure 4. Long-term stability and selectivity of PTNS. (a–c) Transmitted (a), scattering (b), and force images (c) of a single NIH-3T3 cell incubated with cRGD-free PTNS. The scale bar is 10 μm . (d) Time traces of the traction force of PTNS marked in (c). (e–g) Transmitted, (e) force images (f), and the CL488-Paxillin fluorescent images (g) of the representative single NIH-3T3 cell. The scale bar is 10 μm .

Measure the Mechanical Force at Cell–Matrix Adhesion Bonds

We cultivated NIH-3T3 cells, widely utilized in studies on cell adhesion and migration,^{2,40–43} with PTNS for probing cellular mechanical forces (Figure 3a). The AuNP-bound cRGD peptides specifically bound to integrins on the cell membrane (see the Methods section), which were then connected to the F-actin via adapter proteins (talin and vinculin). Traction forces generated by intracellular retrograde F-actin flow were transmitted to the extracellular PTNS through protein–protein interactions, resulting in reduced scattering. In consideration of the large distance between PTNS, the gold surface was also modified with cRGD peptides to promote cell adhesion (see the Methods section).

Figure 3b,c shows the transmitted and scattering images of a single NIH-3T3 cell during the adhesion process. The cell boundary in the scattering image was delineated based on the transmitted image. Due to its minimal scattering cross section in the red-light window, the cell was not visible in the scattering image, enabling us to measure PTNS scattering without biological sample interference. As the cell was under tension, PTNS beneath it was pulled away from the gold surface by F-actin, resulting in weaker scattering compared to neighboring extracellular PTNS (Figure 3c). By applying eq 2 to PTNS scattering beneath the cell, we obtained the force image of the cell (Figure 3d). The highest force, reaching up to 20 pN, was found to exist in the middle and lower-left regions of the cell, while the force in other parts was as low as 2 pN. However, given the size of the AuNP (~ 70 nm), potential false positive signals could arise from other physiological processes such as endocytosis. To validate that the reduced scattering

intensity arose from traction forces, we conducted a series of control experiments. First, the cell in Figure 3b was treated with cytochalasin D, an inhibitor of actin polymerization, to eliminate all mechanical forces.² After 5 min of treatment, actin polymerization was disrupted. It caused the release of pulled PTNS and their scattering to recover, although the boundary did not change much (Figure 3e,f). As a control, the scattering of neighboring PTNS remained stable throughout the process. As shown in Figure 3g, the mean force decreased significantly to less than 2 pN, which is close to the detection limit of PTNS. These results confirmed that cellular mechanical forces contribute to changes in PTNS scattering intensity.

To further prove that the observed mechanical force originated from the traction force rather than endocytosis, we conducted the following control experiments. Figure 4a–c demonstrates the transmitted, scattering, and force images of a single NIH-3T3 cell cultured with PTNS without cRGD ligands. In contrast to cRGD-modified PTNS, only weak forces (~ 1 pN) were measured, similar to those observed under cells treated with cytochalasin D (Figure 3e–g). We selected four PTNS labeled with 1 to 4 beneath the cell to demonstrate their long-term stability. As shown in Figure 4d, there was only a small fluctuation of ± 1 pN in these PTNS, confirming that the forces measured by PTNS in Figure 3d did not originate from endocytosis. We attribute the antiendocytosis property of PTNS to the presence of PEG, commonly used to reduce nonspecific adsorption of nanoparticles on the cell membrane. Further evidence was obtained by performing co-imaging of FAs and PTNS using cells transfected with paxillin markers (for details, see the Methods section). Paxillin is a cytoskeletal protein that is primarily localized to FAs and is highly

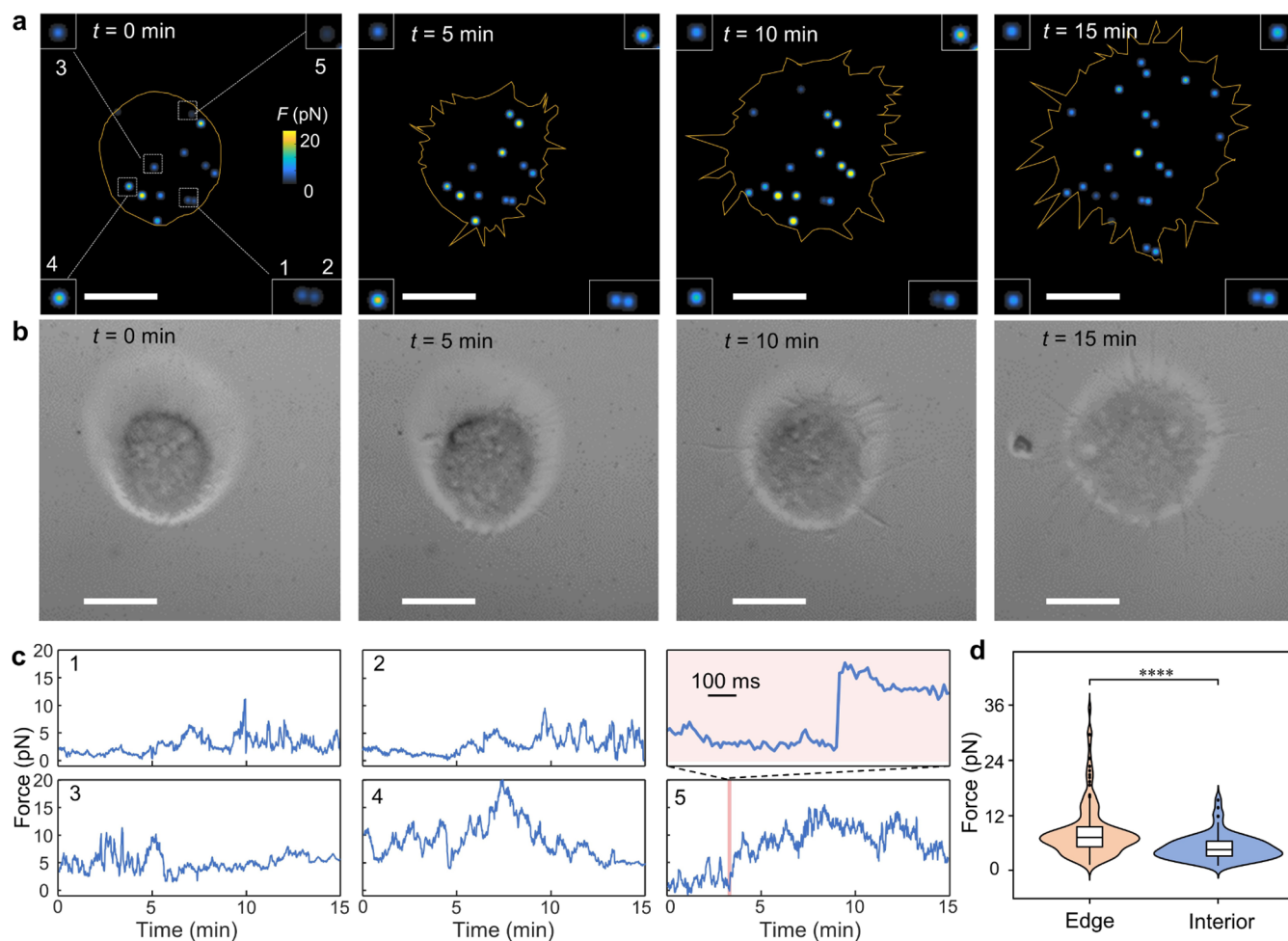


Figure 5. Force transitions during the cell adhesion process. (a, b) Scattering (a) and transmitted images (b) of a single NIH-3T3 cell during the adhesion process. The scale bar is $10 \mu\text{m}$. Insets: magnifications of regions marked with dash boxes. (c) Time traces of the traction force of PTNS marked in (a). Insets: magnification of the region marked with the yellow box. (d) Distributions of the traction force loads on PTNS in different regions of cells (edge: $n = 153$; Interior: $n = 88$). ($****P < 0.0001$).

correlated to the traction force.^{1,4} Figure 4E–G presents transmitted, force, and fluorescent images of the same NIH-3T3 cell. The locations where PTNS exhibited stronger forces which also showed higher fluorescent emission (solid circles), while weaker forces were observed in the areas with low fluorescent emission (dashed circles). These control experiments collectively supported the notion that PTNS can measure traction forces. One concern pertained to the number of linkers between the PTNS and F-actin. To control this, we carefully regulated the density of modified cRGD peptides. Specifically, we used a ratio of alkyne-PEG₂₀₀₀-SH to cRGD of 20:1 to avoid multiple connections between AuNP and integrins (see the Methods section). Our experiments showed that a higher ratio, such as 30:1, resulted in most particles being unable to connect to the cell (Figure S7). While it is challenging to confirm whether each PTNS exclusively has a single cRGD ligand on its top area, the comparatively low density still ensures sole connection since the dimension of AuNP fits well with the average distance between integrins being approximately 70 nm .^{44–46} We acknowledge that the impact of nanostructures on force transmission related to focal adhesions is still a subject of debate. However, our results, at least for NIH-3T3 cells, suggested the feasibility of using

PTNS to measure the traction forces at cell–matrix adhesion bonds.

Measure Transient Force Transitions during the Cell Adhesion Process

We next utilized PTNS to measure the dynamics of the traction forces during the entire process of cell adhesion. In Figure 5a, snapshots of traction force video were presented, showing a single NIH-3T3 cell with monodisperse PTNS during a 15 min cell adhesion process. The transmitted images (Figure 5b) were utilized to define the boundary of the cell in the force image. Following a 10 min adhesion period, the cell expanded quickly and the traction force on PTNS beneath the cell increased, suggesting the formation of adhesion sites by the cell. Nevertheless, the cell boundary stopped changing, and the traction force decreased in the final 5 min as the cell adhesion matured. During this stage, cell adhesion could be maintained with only a small mechanical force, which aligned with previous reports.^{14,47} To illustrate the dynamics of subcellular forces, we chose five PTNS (P-1 to 5) beneath the cell for further studies. As shown in Figure 5c, these PTNS exhibited strong vibrations in the traction force, in contrast to that without cRGD (Figure 4d). Notably, neighboring PTNS often demonstrated synchronized vibration trends such as P-1 and P-2. F-actin is typically cross-linked to form networks, resulting

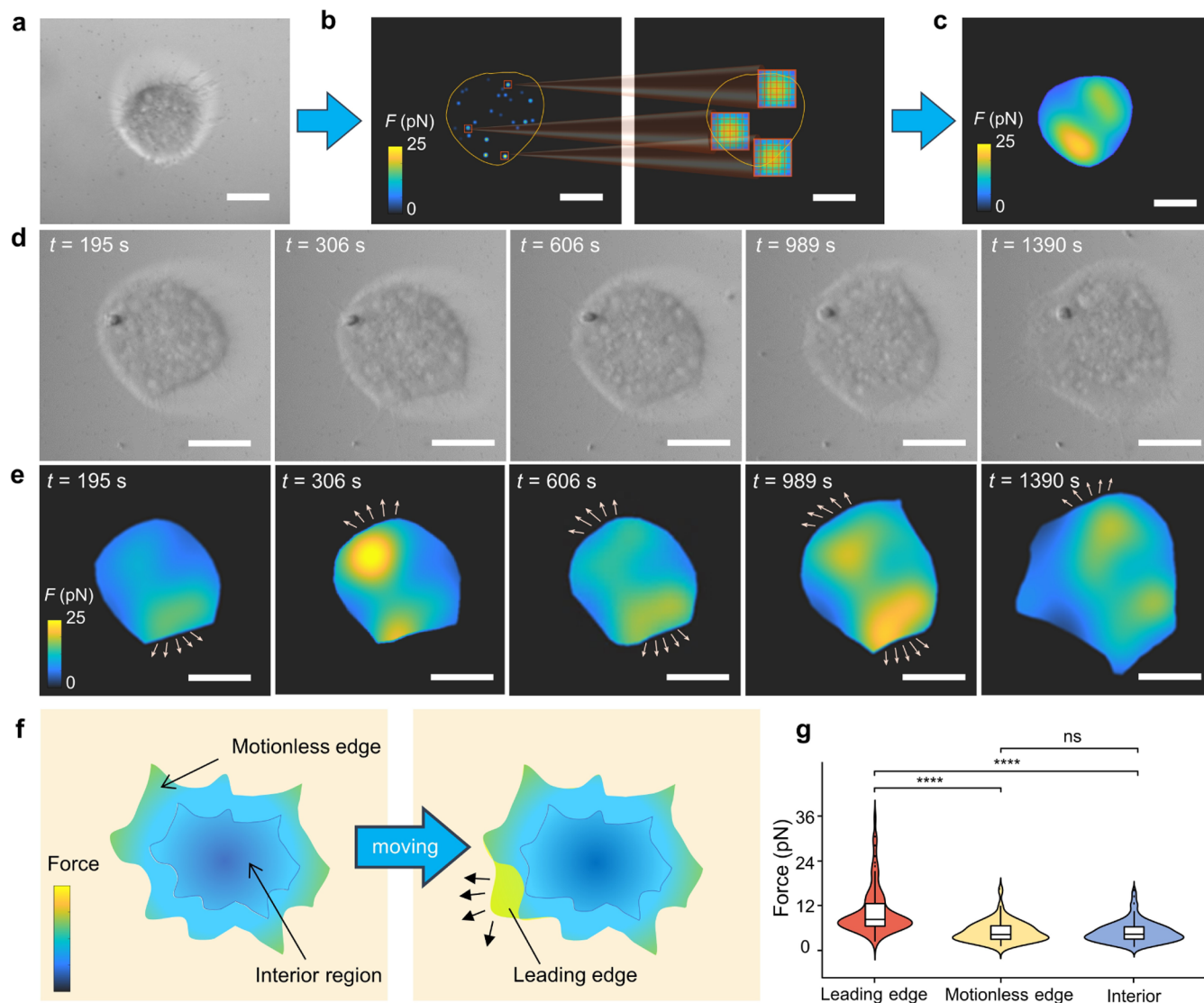


Figure 6. Cell moving direction correlated to traction force. (a–c) Schematic illustration of the block-imaging strategy for the pseudo-force mapping of a single NIH-3T3 cell. Scattering (a) and traction force image (b) of PTNS and the pseudo-force mapping of the cell (c). The scale bar is $10\ \mu\text{m}$. (d, e) Snapshots of transmitted (d) and the corresponding pseudo-force video (e) of a single NIH-3T3 cell. Arrows represent the direction of the cell expansion. The scale bar is $10\ \mu\text{m}$. (f) Schematic illustration of the division of cellular regions. (g) Distribution of the traction forces in different regions of cells (leading edge: $n = 98$; motionless edge: $n = 55$; interior: $n = 89$). Student's *t*-test was used to determine significance (**** $P < 0.0001$, ns: $P > 0.05$).

in the formation of FAs.⁴⁸ Consequently, adjacent PTNS situated within the same FA exhibit similar traction forces. The traction forces were strongly correlated to their respective locations. For instance, P-3 was located in the interior area, while P-4 and P-5 were near the cell boundary. P-4 and P-5 demonstrated much higher traction force than P-3 because the cell had already adhered in the interior region but the edge region was forming adhesion sites. To demonstrate this, we quantified multiple PTNS and observed that the average traction force near the cell boundary was greater than in the interior region (Figure 5d). Importantly, the forces at the cell edge exhibited two primary distributions at 3 and 7 pN, respectively. The forces of approximately 3 pN were comparable to those in the interior region. This can be attributed to the presence of both nascent and mature adhesion sites near the edges. The traction force at nascent adhesion sites typically increased gradually at first, reached a plateau, and decreased as the adhesion site matured and only

required maintenance of substrate anchoring.^{47,49} Therefore, we deduced that the location of the strongest traction force can serve as an indicator of the movement direction of the NIH-3T3 cells.

To validate this, we employed the PTNS to map the distribution of tensile forces throughout the process. Nevertheless, visualizing the force distribution for the entire cell was challenging due to the limited density of PTNS modifications. To overcome this, we improved the imaging mode using a block-imaging strategy. As explained earlier (Figure 5c), neighboring PTNS typically exhibited synchronized force dynamics as they were connected to the same FA. Based on this, we assumed that a single PTNS represents the traction force of a block area rather than that of a single molecular clutch. As shown in Figure 6a,b, a single NIH-3T3 cell was cultured above a uniform single PTNS from the center to the boundary. We calculated the real-time traction force of each PTNS and assigned the force value to a 20-by-20-pixel block

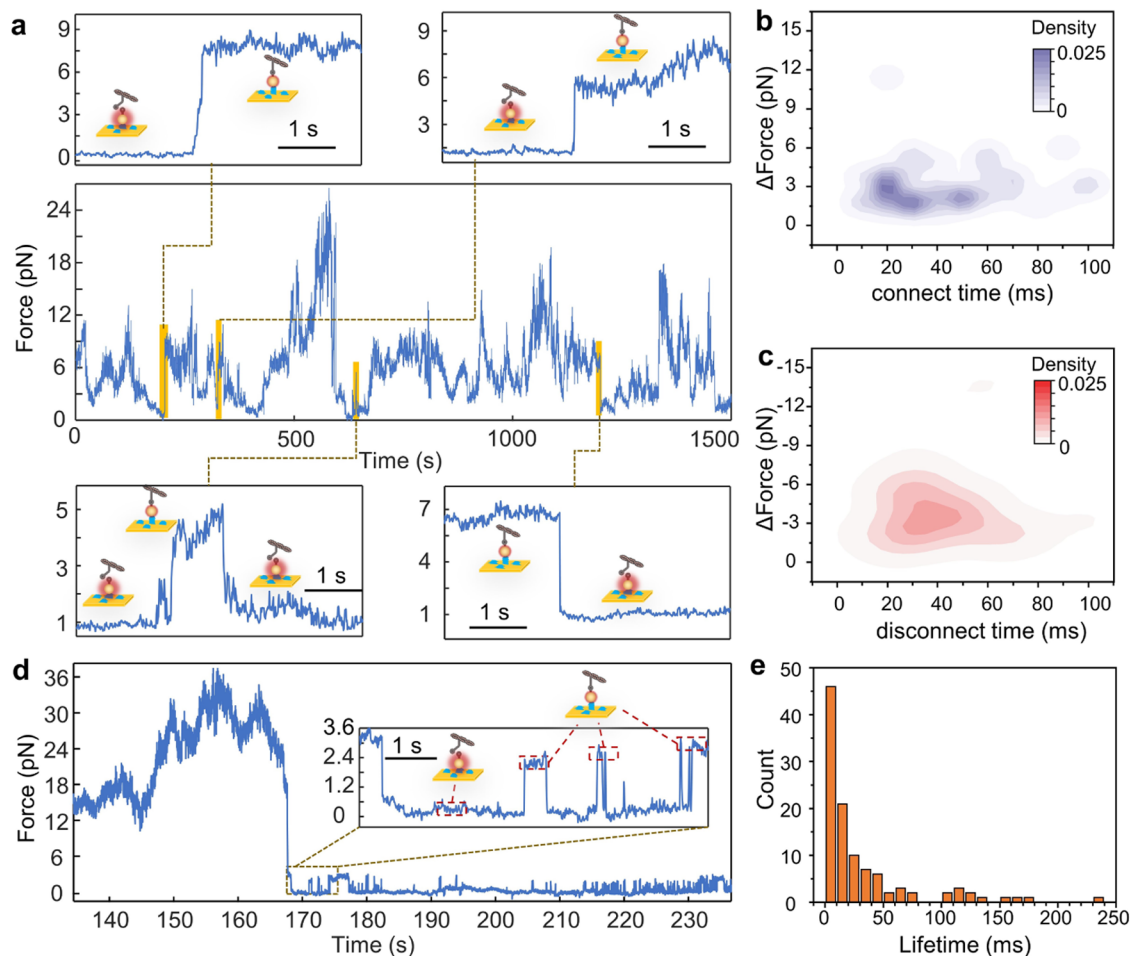


Figure 7. Dynamic step transitions regulated by traction force. (a) Time trace of the traction force load on a single PTNS. Inset: magnifications of instantaneous step transitions marked with yellow boxes. (b, c) Distributions of the force variation and the duration of connection (b) and disconnection (c) transitions (connection: $n = 50$; disconnection: $n = 44$). (d) Time trace of the traction force of a single PTNS with intermittent step transitions. Inset: magnification of the region marked with dashed box. (e) Histogram showing the distribution of the lifetime of intermittent steps ($n = 150$).

around them, which is similar to the area of a single FA. The overlapping blocks generated a pseudo-force mapping for the cell, allowing the examination of local morphodynamics related to dynamic force variations near the cell edge (Figure 6c). Figure 6d,e presents snapshots of transmitted and pseudo-force mapping video (Movie S1), respectively, showing a single cell observed for 25 min. Arrows in the force mapping snapshots represent the leading edge, and the direction of cell expansion is indicated by transmitted images. In each snapshot, the cell showed a significant correlation between the traction force and expansion of the cell edge. The highest force typically occurred at locations approximately $2 \mu\text{m}$ behind the cell edge, consistent with findings reported in the literature.²⁹ It is worth noting that the cell may have multiple expansion directions simultaneously, which was consistent with the multiple maximum points in the force mapping (Figure 6e). As shown in Figure 6f, we divided the cell into three main regions: the leading edge in the moving direction, the motionless edge, and the interior region. We measured over 50 PTNS in each of the three regions and observed that the average mechanical force at the leading edge was higher than that at the motionless edge, resembling that in the interior region (Figure 6g). These results can account for the dual distribution observed in Figure 5d. It is important to note that

there is still debate regarding how the traction force correlates with the movement direction in the literature.^{29,50} Nevertheless, measurements of NIH-3T3 cells demonstrated that the maximum traction force typically occurs at the leading edges during expansion (Figure 6e and Movie S1). Therefore, dynamic changes in the traction force, as assessed in this study, are essential for cell movement.

Measure Single-Molecule Force Transitions at Cell–Matrix Adhesion Bonds

During cellular physiology, forces generated by retrograde F-actin flow are transmitted to the extracellular matrix (ECM) through a series of mechanosensitive protein–protein interactions known as molecular clutches.^{9,16,51,52} Dunn et al. recently developed a modified clutch model and categorized single-molecule tension transitions as gradual ramps or instantaneous step transitions.¹² The time-dependent force curves of our method also exhibited these two types of tension transitions. For instance, the strong vibrations in the traction force curves of P-1 to 5 in Figure 5C corresponded to ramp transitions, which indicated load equilibration within the cross-linked network. By amplifying the force curve of P-5, we can observe stepwise transitions in the force trace. Figure 7a shows more examples of instantaneous step transitions, including

falling and rising steps, indicating the disconnection or reattachment of an individual molecular clutch to F-actin (see also [Movies S2–S5](#)).¹² Step transitions typically occurred at the beginning or end of ramp transitions (more examples in [Figure S8](#)) because attachment to F-actin is necessary for force transmission. The stable force with sporadic ramp and step events was consistent with the prediction of molecular clutch simulations with reversible cross-linkers.¹² To confirm that these step transitions arose from individual clutches, we assayed more than 40 samples for each type of step transition and defined the rising time from 10 to 90% or the falling time from 90 to 10% of the maximum forces as the transition time. [Figure 7b,c](#) illustrates that both connections and disconnections have concentrated distributions in step forces and transition times, supporting the notion that these step transitions originate from individual clutches. A few steps demonstrating larger step forces may arise from multiple connections between AuNP and integrins, although cRGD density on AuNP was carefully controlled (see the [Methods](#) section). Additionally, we observed deviations between connections and disconnections. The connection time showed a concentrated distribution at around 25 ms, while disconnection time typically occurred around 39 ms, suggesting that mechanical activation of integrins modulates bond strength and may induce longer disconnection processes.

Our observations prompted us to explore the disconnection and reattachment of an individual clutch to the F-actin in the absence of traction forces. Once the FAs transitioned from nascent to mature, the force decreased to approximately 1 pN without any ramps ([Figures 5c and 7d](#)). However, we still observed reversible intermittent step transitions of approximately 3 pN in this situation (see also [Movie S6](#)). Given the short lifetimes (<50 ms) and step durations (<30 ms) ([Figures 7e and S9](#)), we attributed these intermittent steps to weak binding between either integrin and the ECM or talin and F-actin in the absence of traction force. Although similar results have been reported in previous *in vitro* single-molecule experiments,^{53–55} our results, obtained from living cells, confirmed that the traction force through the F-actin can regulate the lifetime and transition time of single-molecule clutches. The instantaneous connection of single-molecule clutches is necessary but not sufficient for the equilibration of loads within the cross-linked network. A higher traction force load on F-actin can promote the stable connection of molecular clutches.

CONCLUSIONS

In conclusion, we proposed a new class of tension sensor called PTNS, which is based on the ultrasensitive measurement of the subnanoscale movement of single plasmonic nanoparticles. Compared to the current fluorescence-based MTS, PTNS demonstrates a wide continuous detection range from 1.1 to 48 pN. This performance can be adjusted by controlling the number of poly(ethylene glycol) (PEG) chains under AuNPs, as more chains allow for larger force measurement but may affect the detection limit. The temporal resolution of 10 ms can be improved by using a high-speed camera, although it is already sufficient for cellular mechanical force measurement. Additionally, PTNS, benefiting from robust plasmonic scattering, enables high-throughput tracking of traction force dynamics at individual FAs during long-term cell adhesion or movement processes. PTNS provides a universal tool for studying various biophysical phenomena, including single-

molecule force spectroscopy, mechanosensitive piezo channels, and cellular functions. Moreover, based on PTNS, it is possible to develop imaging devices for drug analysis based on changes in cellular traction force, such as real-time analysis of cancer cellular mechanical force after adding anticancer drugs, to provide more parameters for drug efficacy.

ASSOCIATED CONTENT

Supporting Information

The Supporting Information is available free of charge at <https://pubs.acs.org/doi/10.1021/jacsau.4c00002>.

Experimental detail; chemicals; synthesis of gold nanoparticles; measurement of gap distance-dependent scattering of single gold nanoparticles; finite-difference time-domain simulation; fabrication of plasmonic-coupled tension nanosensor; calibration of the correlation between the tensile force and relative scattering intensity; and cell culture ([Figures S1–S10](#)) ([PDF](#))
Pseudo-force video of the cell in [Figure 6e](#) ([Movie S1](#)) ([MP4](#))

Time-lapse force on a single PTNS in the top left panel of [Figure 7a](#) ([Movie S2](#)) ([MP4](#))

Time-lapse force on a single PTNS in the top right panel of [Figure 7a](#) ([Movie S3](#)) ([MP4](#))

Time-lapse force on a single PTNS in the bottom left panel of [Figure 7a](#) ([Movie S4](#)) ([MP4](#))

Time-lapse force on a single PTNS in the bottom right panel of [Figure 7a](#) ([Movie S5](#)) ([MP4](#))

Time-lapse force on a single PTNS in the inset of [Figure 7d](#) ([Movie S6](#)) ([MP4](#))

AUTHOR INFORMATION

Corresponding Authors

Peng Zheng – State Key Laboratory of Analytical Chemistry for Life Science, School of Chemistry and Chemical Engineering, Nanjing University, Nanjing 210023, P. R. China; orcid.org/0000-0003-4792-6364; Email: pengz@nju.edu.cn

Zixuan Chen – State Key Laboratory of Analytical Chemistry for Life Science, School of Chemistry and Chemical Engineering, Nanjing University, Nanjing 210023, P. R. China; orcid.org/0000-0002-3017-1121; Email: chenzixuan@nju.edu.cn

Jun-Jie Zhu – State Key Laboratory of Analytical Chemistry for Life Science, School of Chemistry and Chemical Engineering, Nanjing University, Nanjing 210023, P. R. China; orcid.org/0000-0002-8201-1285; Email: jjzhu@nju.edu.cn

Authors

Shaojun Wu – State Key Laboratory of Analytical Chemistry for Life Science, School of Chemistry and Chemical Engineering, Nanjing University, Nanjing 210023, P. R. China

Wenjing Tang – State Key Laboratory of Analytical Chemistry for Life Science, School of Chemistry and Chemical Engineering, Nanjing University, Nanjing 210023, P. R. China

Ziyi Wang – State Key Laboratory of Analytical Chemistry for Life Science, School of Chemistry and Chemical Engineering, Nanjing University, Nanjing 210023, P. R. China

Zhuodong Tang – State Key Laboratory of Analytical Chemistry for Life Science, School of Chemistry and Chemical Engineering, Nanjing University, Nanjing 210023, P. R. China; orcid.org/0009-0006-2761-5031

Complete contact information is available at:
<https://pubs.acs.org/10.1021/jacsau.4c00002>

Author Contributions

[†]S.W. and W.T. contributed equally to this work. The manuscript was written through contributions of all authors. All authors have given approval to the final version of the manuscript.

Notes

The authors declare no competing financial interest.

ACKNOWLEDGMENTS

This research was supported by National Natural Science Foundation of China (grants nos. 22122405, 22174061, and 22374072), the Central University Basic Research Fund of China (grant nos. 0205119006 and 020514380307), and the program A/B for Outstanding PhD candidate of Nanjing University.

ABBREVIATIONS

MTS, molecular tension sensors; PTNS, plasmonic-coupled tension nanosensor; F-actin, filamentous actin; ECM, extracellular matrix; FAs, focal adhesions; FRET, fluorescence resonance energy transfer; AuNP, gold nanoparticle; WLC, worm-like chain; AFM, atomic force microscope; SMFS, single-molecule force spectroscopy; SPP, surface plasmon polariton; CuAAC, copper-catalyzed azide-alkyne cycloaddition

REFERENCES

- (1) Liu, Y.; Yehl, K.; Narui, Y.; Salaita, K. Tension Sensing Nanoparticles for Mechano-Imaging at the Living/Nonliving Interface. *J. Am. Chem. Soc.* **2013**, *135* (14), 5320–5323.
- (2) Liu, Y.; Medda, R.; Liu, Z.; Galior, K.; Yehl, K.; Spatz, J. P.; Cavalcanti-Adam, E. A.; Salaita, K. Nanoparticle Tension Probes Patterned at the Nanoscale: Impact of Integrin Clustering on Force Transmission. *Nano Lett.* **2014**, *14* (10), 5539–5546.
- (3) Grashoff, C.; Hoffman, B. D.; Brenner, M. D.; Zhou, R.; Parsons, M.; Yang, M. T.; McLean, M. A.; Sligar, S. G.; Chen, C. S.; Ha, T.; Schwartz, M. A. Measuring mechanical tension across vinculin reveals regulation of focal adhesion dynamics. *Nature* **2010**, *466* (7303), 263–266.
- (4) Morimatsu, M.; Mekhdjian, A. H.; Chang, A. C.; Tan, S. J.; Dunn, A. R. Visualizing the Interior Architecture of Focal Adhesions with High-Resolution Traction Maps. *Nano Lett.* **2015**, *15* (4), 2220–2228.
- (5) van Helvert, S.; Storm, C.; Friedl, P. Mechanoreciprocity in cell migration. *Nat. Cell Biol.* **2018**, *20* (1), 8–20.
- (6) Friedrichs, J.; Helenius, J.; Muller, D. J. Quantifying cellular adhesion to extracellular matrix components by single-cell force spectroscopy. *Nat. Protoc.* **2010**, *5* (7), 1353–1361.
- (7) Omidvar, R.; Tafazzoli-shadpour, M.; Shokrgozar, M. A.; Rostami, M. Atomic force microscope-based single cell force spectroscopy of breast cancer cell lines: An approach for evaluating cellular invasion. *J. Biomech.* **2014**, *47* (13), 3373–3379.
- (8) Matellan, C.; del Río Hernández, A. E. Where No Hand Has Gone Before: Probing Mechanobiology at the Cellular Level. *ACS Biomater. Sci. Eng.* **2019**, *5* (8), 3703–3719.

(9) Case, L. B.; Waterman, C. M. Integration of actin dynamics and cell adhesion by a three-dimensional, mechanosensitive molecular clutch. *Nat. Cell Biol.* **2015**, *17* (8), 955–963.

(10) Zhao, B.; O'Brien, C.; Mudiyansele, A. P. K. K.; Li, N.; Bagheri, Y.; Wu, R.; Sun, Y.; You, M. Visualizing Intercellular Tensile Forces by DNA-Based Membrane Molecular Probes. *J. Am. Chem. Soc.* **2017**, *139* (50), 18182–18185.

(11) Zhao, Y.; Pal, K.; Tu, Y.; Wang, X. Cellular Force Nanoscopy with 50 nm Resolution Based on Integrin Molecular Tension Imaging and Localization. *J. Am. Chem. Soc.* **2020**, *142* (15), 6930–6934.

(12) Tan, S. J.; Chang, A. C.; Anderson, S. M.; Miller, C. M.; Prahll, L. S.; Odde, D. J.; Dunn, A. R. Regulation and dynamics of force transmission at individual cell-matrix adhesion bonds. *Sci. Adv.* **2020**, *6* (20), No. eaax0317.

(13) Dutta, P. K.; Zhang, Y.; Blanchard, A. T.; Ge, C.; Rushdi, M.; Weiss, K.; Zhu, C.; Ke, Y.; Salaita, K. Programmable Multivalent DNA-Origami Tension Probes for Reporting Cellular Traction Forces. *Nano Lett.* **2018**, *18* (8), 4803–4811.

(14) Zhang, Y.; Ge, C.; Zhu, C.; Salaita, K. DNA-based digital tension probes reveal integrin forces during early cell adhesion. *Nat. Commun.* **2014**, *5* (1), No. 5167.

(15) Li, H.; Zhang, C.; Hu, Y.; Liu, P.; Sun, F.; Chen, W.; Zhang, X.; Ma, J.; Wang, W.; Wang, L.; Wu, P.; Liu, Z. A reversible shearing DNA probe for visualizing mechanically strong receptors in living cells. *Nat. Cell Biol.* **2021**, *23* (6), 642–651.

(16) Chan, C. E.; Odde, D. J. Traction Dynamics of Filopodia on Compliant Substrates. *Science* **2008**, *322* (5908), 1687–1691.

(17) Zhang, Y.; Yang, C.; Peng, S.; Ling, J.; Chen, P.; Ma, Y.; Wang, W.; Chen, Z.; Chen, C. General Strategy To Improve the Photon Budget of Thiol-Conjugated Cyanine Dyes. *J. Am. Chem. Soc.* **2023**, *145* (7), 4187–4198.

(18) Chen, Z.; Li, J.; Chen, X.; Cao, J.; Zhang, J.; Min, Q.; Zhu, J.-J. Single Gold@Silver Nanoprobes for Real-Time Tracing the Entire Autophagy Process at Single-Cell Level. *J. Am. Chem. Soc.* **2015**, *137* (5), 1903–1908.

(19) Chen, X.; Xia, Q.; Cao, Y.; Min, Q.; Zhang, J.; Chen, Z.; Chen, H.-Y.; Zhu, J.-J. Imaging the transient heat generation of individual nanostructures with a mechanoresponsive polymer. *Nat. Commun.* **2017**, *8* (1), No. 1498.

(20) Xia, Q.; Chen, Z.; Xiao, P.; Wang, M.; Chen, X.; Zhang, J.-R.; Chen, H.-Y.; Zhu, J.-J. Fermi level-tuned optics of graphene for attocoulomb-scale quantification of electron transfer at single gold nanoparticles. *Nat. Commun.* **2019**, *10* (1), No. 3849.

(21) Lee, K.; Cui, Y.; Lee, L. P.; Irudayaraj, J. Quantitative imaging of single mRNA splice variants in living cells. *Nat. Nanotechnol.* **2014**, *9* (6), 474–480.

(22) Wang, H.; Tang, Z.; Wang, Y.; Ma, G.; Tao, N. Probing Single Molecule Binding and Free Energy Profile with Plasmonic Imaging of Nanoparticles. *J. Am. Chem. Soc.* **2019**, *141* (40), 16071–16078.

(23) Fang, Y.; Chen, S.; Wang, W.; Shan, X.; Tao, N. Real-Time Monitoring of Phosphorylation Kinetics with Self-Assembled Nanoscissors. *Angew. Chem., Int. Ed.* **2015**, *54* (8), 2538–2542.

(24) Shan, X.; Fang, Y.; Wang, S.; Guan, Y.; Chen, H.-Y.; Tao, N. Detection of Charges and Molecules with Self-Assembled Nano-Oscillators. *Nano Lett.* **2014**, *14* (7), 4151–4157.

(25) Chen, Z.; Peng, Y.; Cao, Y.; Wang, H.; Zhang, J.-R.; Chen, H.-Y.; Zhu, J.-J. Light-Driven Nano-oscillators for Label-Free Single-Molecule Monitoring of MicroRNA. *Nano Lett.* **2018**, *18* (6), 3759–3765.

(26) Rooin-Peikar, M.; Xu, Q.; Wang, X.; Ha, T. Ultrasensitivity of Cell Adhesion to the Presence of Mechanically Strong Ligands. *Phys. Rev. X* **2016**, *6* (1), No. 011001.

(27) Liu, Y.; Blanchfield, L.; Ma, V. P.-Y.; Andargachew, R.; Galior, K.; Liu, Z.; Evavold, B.; Salaita, K. DNA-based nanoparticle tension sensors reveal that T-cell receptors transmit defined pN forces to their antigens for enhanced fidelity. *Proc. Natl. Acad. Sci. U.S.A.* **2016**, *113* (20), 5610–5615.

(28) Chang, A. C.; Mekhdjian, A. H.; Morimatsu, M.; Denisin, A. K.; Pruitt, B. L.; Dunn, A. R. Single Molecule Force Measurements in

- Living Cells Reveal a Minimally Tensioned Integrin State. *ACS Nano* **2016**, *10* (12), 10745–10752.
- (29) Nordenfelt, P.; Elliott, H. L.; Springer, T. A. Coordinated integrin activation by actin-dependent force during T-cell migration. *Nat. Commun.* **2016**, *7* (1), No. 13119.
- (30) Zhang, P.; Zhou, L.; Wang, R.; Zhou, X.; Jiang, J.; Wan, Z.; Wang, S. Evanescent scattering imaging of single protein binding kinetics and DNA conformation changes. *Nat. Commun.* **2022**, *13* (1), No. 2298.
- (31) Zhang, P.; Ma, G.; Dong, W.; Wan, Z.; Wang, S.; Tao, N. Plasmonic scattering imaging of single proteins and binding kinetics. *Nat. Methods* **2020**, *17* (10), 1010–1017.
- (32) Mock, J. J.; Hill, R. T.; Degiron, A.; Zauscher, S.; Chilkoti, A.; Smith, D. R. Distance-Dependent Plasmon Resonant Coupling between a Gold Nanoparticle and Gold Film. *Nano Lett.* **2008**, *8* (8), 2245–2252.
- (33) Deng, Y.; Wu, T.; Wang, M.; Shi, S.; Yuan, G.; Li, X.; Chong, H.; Wu, B.; Zheng, P. Enzymatic biosynthesis and immobilization of polypeptide verified at the single-molecule level. *Nat. Commun.* **2019**, *10* (1), No. 2775.
- (34) Krupička, M.; Dopieralski, P.; Marx, D. Unlicking the Click: Metal-Assisted Mechanochemical Cycloreversion of Triazoles Is Possible. *Angew. Chem., Int. Ed.* **2017**, *56* (27), 7745–7749.
- (35) Ratto, T. V.; Rudd, R. E.; Langry, K. C.; Balhorn, R. L.; McElfresh, M. W. Nonlinearly Additive Forces in Multivalent Ligand Binding to a Single Protein Revealed with Force Spectroscopy. *Langmuir* **2006**, *22* (4), 1749–1757.
- (36) Seifert, U. Rupture of Multiple Parallel Molecular Bonds under Dynamic Loading. *Phys. Rev. Lett.* **2000**, *84* (12), 2750–2753.
- (37) Nie, J.; Deng, Y.; Tian, F.; Shi, S.; Zheng, P. Detection of weak non-covalent cation- π interactions in NGAL by single-molecule force spectroscopy. *Nano Res.* **2022**, *15* (5), 4251–4257.
- (38) Song, G.; Ding, X.; Liu, H.; Yuan, G.; Tian, F.; Shi, S.; Yang, Y.; Li, G.; Zheng, P. Single-Molecule Force Spectroscopy Reveals that the Fe–N Bond Enables Multiple Rupture Pathways of the 2Fe2S Cluster in a MitoNEET Monomer. *Anal. Chem.* **2020**, *92* (21), 14783–14789.
- (39) Flory, P. *Statistical Mechanics of Chain Molecules*; Hanser: Munich, 1970; Vol. 401, pp 307–338.
- (40) Hippler, M.; Weißenbruch, K.; Richler, K.; Lemma, E. D.; Nakahata, M.; Richter, B.; Barner-Kowollik, C.; Takashima, Y.; Harada, A.; Blasco, E.; Wegener, M.; Tanaka, M.; Bastmeyer, M. Mechanical stimulation of single cells by reversible host-guest interactions in 3D microstructures. *Sci. Adv.* **2020**, *6* (39), No. eabc2648.
- (41) Hennig, K.; Wang, I.; Moreau, P.; Valon, L.; DeBeco, S.; Coppey, M.; Miroshnikova, Y. A.; Albiges-Rizo, C.; Favard, C.; Voituriez, R.; Balland, M. Stick-slip dynamics of cell adhesion triggers spontaneous symmetry breaking and directional migration of mesenchymal cells on one-dimensional lines. *Sci. Adv.* **2020**, *6* (1), No. eaau5670.
- (42) Brockman, J. M.; Blanchard, A. T.; Pui-Yan, V.; Derricotte, W. D.; Zhang, Y.; Fay, M. E.; Lam, W. A.; Evangelista, F. A.; Mattheyses, A. L.; Salaita, K. Mapping the 3D orientation of piconewton integrin traction forces. *Nat. Methods* **2018**, *15* (2), 115–118.
- (43) Oakes, P. W.; Wagner, E.; Brand, C. A.; Probst, D.; Linke, M.; Schwarz, U. S.; Glotzer, M.; Gardel, M. L. Optogenetic control of RhoA reveals zyxin-mediated elasticity of stress fibres. *Nat. Commun.* **2017**, *8* (1), No. 15817.
- (44) Poole, K.; Khairy, K.; Friedrichs, J.; Franz, C.; Cisneros, D. A.; Howard, J.; Mueller, D. Molecular-scale Topographic Cues Induce the Orientation and Directional Movement of Fibroblasts on Two-dimensional Collagen Surfaces. *J. Mol. Biol.* **2005**, *349* (2), 380–386.
- (45) Arnold, M.; Hirschfeld-Warneken, V. C.; Lohmüller, T.; Heil, P.; Blümmel, J.; Cavalcanti-Adam, E. A.; López-García, M.; Walther, P.; Kessler, H.; Geiger, B.; Spatz, J. P. Induction of Cell Polarization and Migration by a Gradient of Nanoscale Variations in Adhesive Ligand Spacing. *Nano Lett.* **2008**, *8* (7), 2063–2069.
- (46) Huang, J.; Gräter, S. V.; Corbellini, F.; Rinck, S.; Bock, E.; Kenkemer, R.; Kessler, H.; Ding, J.; Spatz, J. P. Impact of Order and Disorder in RGD Nanopatterns on Cell Adhesion. *Nano Lett.* **2009**, *9* (3), 1111–1116.
- (47) Beningo, K. A.; Dembo, M.; Kaverina, I.; Small, J. V.; Wang, Y.-l. Nascent Focal Adhesions Are Responsible for the Generation of Strong Propulsive Forces in Migrating Fibroblasts. *J. Cell Biol.* **2001**, *153* (4), 881–888.
- (48) Gardel, M. L.; Shin, J. H.; MacKintosh, F. C.; Mahadevan, L.; Matsudaira, P.; Weitz, D. A. Elastic Behavior of Cross-Linked and Bundled Actin Networks. *Science* **2004**, *304* (5675), 1301–1305.
- (49) Gardel, M. L.; Sabass, B.; Ji, L.; Danuser, G.; Schwarz, U. S.; Waterman, C. M. Traction stress in focal adhesions correlates biphasically with actin retrograde flow speed. *J. Cell Biol.* **2008**, *183* (6), 999–1005.
- (50) Mehidi, A.; Kage, F.; Karatas, Z.; Cercy, M.; Schaks, M.; Poleskaya, A.; Sainlos, M.; Gautreau, A. M.; Rossier, O.; Rottner, K.; Giannone, G. Forces generated by lamellipodial actin filament elongation regulate the WAVE complex during cell migration. *Nat. Cell Biol.* **2021**, *23* (11), 1148–1162.
- (51) Oriá, R.; Wiegand, T.; Escribano, J.; Elosegui-Artola, A.; Uriarte, J. J.; Moreno-Pulido, C.; Platzman, I.; Delcanale, P.; Albertazzi, L.; Navajas, D.; Trepát, X.; García-Aznar, J. M.; Cavalcanti-Adam, E. A.; Roca-Cusachs, P. Force loading explains spatial sensing of ligands by cells. *Nature* **2017**, *552* (7684), 219–224.
- (52) Elosegui-Artola, A.; Oriá, R.; Chen, Y.; Kosmalka, A.; Pérez-González, C.; Castro, N.; Zhu, C.; Trepát, X.; Roca-Cusachs, P. Mechanical regulation of a molecular clutch defines force transmission and transduction in response to matrix rigidity. *Nat. Cell Biol.* **2016**, *18* (5), 540–548.
- (53) Friedland, J. C.; Lee, M. H.; Boettiger, D. Mechanically Activated Integrin Switch Controls $\alpha 5 \beta 1$ Function. *Science* **2009**, *323* (5914), 642–644.
- (54) Kong, F.; Li, Z.; Parks, W. M.; Dumbauld, D. W.; García, A. J.; Mould, A. P.; Humphries, M. J.; Zhu, C. Cyclic Mechanical Reinforcement of Integrin–Ligand Interactions. *Mol. Cell* **2013**, *49* (6), 1060–1068.
- (55) Owen, L. M.; Bax, N. A.; Weis, W. I.; Dunn, A. R. The C-terminal actin-binding domain of talin forms an asymmetric catch bond with F-actin. *Proc. Natl. Acad. Sci. U.S.A.* **2022**, *119* (10), No. e2109329119.